Energies **2013**, *6*, 1233-1249; doi:10.3390/en6031233

OPEN ACCESS

energies

ISSN 1996-1073

www.mdpi.com/journal/energies

Article

Characteristics of Methane Hydrate Formation in Artificial and Natural Media

Peng Zhang *, Qingbai Wu and Yuzhong Yang

State Key Laboratory of Frozen Soil Engineering, Cold and Arid Regions Environmental and Engineering Research Institute, Chinese Academy of Sciences, Lanzhou 730000, Gansu, China; E-Mails: qbwu@lzb.ac.cn (Q.W.); yangyuzhong08@live.cn (Y.Y.)

* Author to whom correspondence should be addressed; E-Mail: zhangpeng@lzb.ac.cn; Tel.: +86-931-4967887; Fax: +86-931-4967284.

Received: 20 December 2012; in revised form: 29 January 2013 / Accepted: 4 February 2013 / Published: 1 March 2013

Abstract: The formation of methane hydrate in two significantly different media was investigated, using silica gel as an artificial medium and loess as a natural medium. The methane hydrate formation was observed through the depletion of water in the matrix, measured via the matrix potential and the relationship between the matrix potential and the water content was determined using established equations. The velocity of methane hydrate nucleation slowed over the course of the reaction, as it relied on water transfer to the hydrate surfaces with lower Gibbs free energy after nucleation. Significant differences in the reactions in the two types of media arose from differences in the water retention capacity and lithology of media due to the internal surface area and pore size distributions. Compared with methane hydrate formation in silica gel, the reaction in loess was much slower and formed far less methane hydrate. The results of this study will advance the understanding of how the properties of the environment affect the formation of gas hydrates in nature.

Keywords: water conversion; matrix potential; methane hydrate; porous media

---

1. Introduction

Natural gas hydrates are non-stoichiometric compounds consisting of small gas molecules fitted into polyhedral water cavities [1] and have been found throughout the World in a variety of locations, including on land under permafrost, offshore under the sea floor, and in sediments of deep lakes [2]. Natural gas hydrates are potential energy sources because of the naturally present enormous amount and the growing demand for natural gas [3,4]. In nature, most natural gas hydrates exist in the form of inclusions within sediment or cemented soils, with only 6% present in bulk form. As the surrounding environment significantly influences natural gas hydrate formation, understanding the thermodynamic mechanism underlying the formation of natural gas hydrates in porous media is instrumental to research on gas hydrate storage [5]. Handa and Stupin [5] pioneered the effort to characterize pore size effects on hydrate equilibrium conditions in porous media, opening the way for many other researchers to refine and expand their work, not only on experiments [6–16], but also from theoretical points of view [17–22].

A review of the literature revealed that much attention had been given to the conditions under which natural gas hydrates are present in sediments, but that the relevant formation and dissociation processes had been largely ignored. On this basis, we undertook the characterization of the hydrate formation process as observed through the water conversion ratios. Several reports in the literature [23–26] describe the dynamics of water in sediments, confirming that formation processes in porous media are always accompanied by water transfer behavior. Unfortunately, no quantitative studies of such water process have been performed, nor are there any reports characterizing natural gas hydrate formation based on water conversion ratios present in the literature.

In this report, gas hydrate formation in two types of porous media was quantitated by measuring the extent of water conversion via matrix potentials. The matrix potential was defined as in agrology, corresponding with the suction by the complicated physical properties of water within a soil matrix; in results from the water adsorption and the capillary function derived from the soil micro particles and can be quantitatively measured. Establishing the relationship between matrix potential and methane hydrate formation in different types of porous media has the potential to substantially advance research on gas hydrates.

2. Experimental

2.1. Experimental Media

In this study, an artificial medium-consisting of silica gel (Shangbang Industrial Co., Ltd., Shanghai) and a natural medium-consisting of loess (sampled at a depth of 1.5 meters underground in Yuzhong County in Lanzhou, China) were chosen for comparison due to their widely differing properties. The physical properties of the media are listed in Table 1, in which both “particle size” and “pore size” parameters have the same sources as those listed in Tables 2 and 3, all of them are from BJH Adsorption Pore Distribution Reports, and those in Table 1 are just the average.

Table 1. Physical properties of the experimental media.

Media	Average particle size (μm)	Average pore size (nm)	Media mass (g)	Water content (g)	Experimental water content (%)	Saturated water content (%)	Media density (g/cm^3)
Silica	25–58	6.588	600.0	600.0	100.0	140.0	0.518
Loess	34.5	13.499	1100.0	198.0	18.0	25.0	1.148

Table 2. Pore distribution characteristics of silica gel powder.

BJH Adsorption Pore Distribution Report on Silica Gel Powder							
Pore Width (Å)	Average Width (Å)	Incremental Pore Volume (cm^3/g)	Cumulative Pore Volume (cm^3/g)	Incremental/ Total (%)	Cumulative/ Total (%)	Incremental Pore Area (cm^2/g)	Cumulative Pore Area (cm^2/g)
2470.3–869.5	1039.478	0.00302671	0.00302671	0.43	0.43	0.116470273	0.116470273
869.5–350.3	418.734	0.00268302	0.00570973	0.38	0.80	0.25629843	0.372768703
350.3–215.2	250.694	0.00262260	0.00833234	0.37	1.17	0.418454692	0.791223396
215.2–141.0	162.259	0.01324543	0.02157778	1.86	3.04	3.265239322	4.056462717
141.0–116.5	126.201	0.03524707	0.05682485	4.96	7.99	11.17163684	15.22809956
116.5–95.0	103.342	0.08837089	0.14519575	12.43	20.43	34.20494771	49.43304727
95.0–81.7	87.245	0.09188420	0.23707995	12.93	33.36	42.12650457	91.55955184
81.7–71.3	75.718	0.08788839	0.32496834	12.37	45.72	46.42896269	137.9885145
71.3–62.9	66.501	0.07522551	0.40019385	10.58	56.31	45.24757278	183.2360873
62.9–55.8	58.852	0.06330304	0.46349690	8.91	65.21	43.02463044	226.2607177
55.8–50.9	53.106	0.04239892	0.50589582	5.97	71.18	31.93511904	258.1958368
50.9–46.6	48.563	0.03623140	0.54212722	5.10	76.27	29.84240283	288.0382396
46.6–42.7	44.453	0.03141543	0.57354266	4.42	80.69	28.26787886	316.3061185
42.7–39.2	40.761	0.02580092	0.59934358	3.63	84.32	25.31895638	341.6250749
39.2–36.1	37.516	0.02120234	0.62054592	2.98	87.31	22.60602898	364.2311038
36.1–33.3	34.599	0.01797882	0.63852475	2.53	89.84	20.78480393	385.0159078
33.3–30.9	32.008	0.01434690	0.65287165	2.02	91.86	17.92910236	402.9450101
30.9–28.6	29.646	0.01228466	0.66515632	1.73	93.58	16.57461994	419.5196301
28.6–26.7	27.585	0.00946200	0.67461833	1.33	94.92	13.72013228	433.2397624

Table 2. *Cont.*

BJH Adsorption Pore Distribution Report on Silica Gel Powder							
Pore Width (Å)	**Average Width (Å)**	**Incremental Pore Volume (cm^3/g)**	**Cumulative Pore Volume (cm^3/g)**	**Incremental /Total (%)**	**Cumulative /Total (%)**	**Incremental Pore Area (cm^2/g)**	**Cumulative Pore Area (cm^2/g)**
26.7–24.7	25.608	0.00930031	0.68391865	1.31	96.22	14.52678086	447.7665432
24.7–22.8	23.643	0.00782113	0.69173978	1.10	97.32	13.23193489	460.9984781
22.8–21.0	21.813	0.00642211	0.69816190	0.90	98.23	11.77642293	472.774901
21.0–19.8	20.337	0.00421730	0.70237920	0.59	98.82	8.294695819	481.0695969
19.8–18.5	19.052	0.00386078	0.70623998	0.54	99.36	8.105405224	489.1750021
18.5–17.6	18.026	0.00233290	0.70857288	0.33	99.69	5.176485054	494.3514871
17.6–16.9	17.223	0.002183679	0.71075656	0.31	100.00	5.071311594	499.4227987

Table 3. Pore distribution characteristics of loess.

BJH Adsorption Pore Distribution Report on Loess							
Pore Width (Å)	**Average Width (Å)**	**Incremental Pore Volume (cm^3/g)**	**Cumulative Pore Volume (cm^3/g)**	**Incremental /Total (%)**	**Cumulative /Total (%)**	**Incremental Pore Area (cm^2/g)**	**Cumulative Pore Area (cm^2/g)**
1869.4–493.3	577.3446	0.010181245	0.010181245	46.48	40.88	0.705384178	0.705384178
493.3–274.7	324.3651	0.00423548	0.014416734	19.34	57.89	0.52231128	1.227695463
274.7–187.5	214.2821	0.00221269	0.016629427	10.10	66.78	0.41304279	1.640738257
187.5–143.1	159.0460	0.00131285	0.017942278	5.99	72.05	0.33018134	1.970919598
143.1–115.2	125.9573	0.00096664	0.018908918	4.41	75.93	0.30697376	2.277893358
115.2–95.8	103.5476	0.00077629	0.019685207	3.54	79.05	0.29987731	2.577770676
95.8–82.4	87.99569	0.00062284	0.02030805	2.84	81.55	0.28312426	2.86089494
82.4–71.7	76.20210	0.00053668	0.020844737	2.45	83.71	0.28171729	3.142612236
71.7–63.5	67.03464	0.00042858	0.021273317	1.96	85.43	0.25573681	3.398349051
63.5–56.7	59.64251	0.00037800	0.02165132	1.73	86.94	0.25351235	3.651861407
56.7–51.3	53.64976	0.00032116	0.021972481	1.47	88.23	0.23945019	3.891311603
51.3–46.4	48.52991	0.00029699	0.022269472	1.36	89.43	0.24478997	4.136101573

Table 3. *Cont.*

BJH Adsorption Pore Distribution Report on Loess							
Pore Width (Å)	**Average Width (Å)**	**Incremental Pore Volume (cm^3/g)**	**Cumulative Pore Volume (cm^3/g)**	**Incremental /Total (%)**	**Cumulative /Total (%)**	**Incremental Pore Area (cm^2/g)**	**Cumulative Pore Area (cm^2/g)**
46.4–42.5	44.22794	0.00024723	0.022516707	1.13	90.42	0.22360066	4.359702234
42.5–38.9	40.51761	0.00024431	0.022761021	1.12	91.40	0.24119308	4.600895316
38.9–35.8	37.21000	0.00022531	0.022986331	1.03	92.31	0.24220341	4.843098727
35.8–33.1	34.31840	0.00023468	0.023221011	1.07	93.25	0.27353267	5.116631401
33.1–30.4	31.61019	0.00023952	0.02346054	1.09	94.21	0.30310342	5.419734829
30.4–28.2	29.17505	0.00021903	0.023679572	1.00	95.09	0.30029990	5.72003473
28.2–26.2	27.07171	0.00022227	0.023901843	1.01	95.98	0.32841759	6.04845233
26.2–24.1	25.04651	0.00022170	0.024123548	1.01	96.87	0.35406993	6.402522262
24.1–22.4	23.15869	0.00020903	0.024332587	0.95	97.71	0.36105545	6.763577712
22.4–20.5	21.35191	0.00019146	0.024524047	0.87	98.48	0.35867440	7.122252119
20.5–19.3	19.86598	0.00015711	0.024681159	0.72	99.11	0.31634431	7.438596433
19.3–18.0	18.58923	0.00012330	0.024804463	0.56	99.61	0.26532155	7.703917983
18.0–17.3	17.61015	0.00009792	0.024902387	0.45	100.00	0.22242658	7.926344567

2.2. Experimental Method

Using an apparatus designed and assembled in house (Figure 1), methane hydrate was formed within the media and the water conversion ratios during the reaction were determined. Distilled water was combined with each of the experimental media by stirring (Table 1), and then placed into the reaction cell, which was a stainless steel cylinder (height 19.5 cm, diameter 10.0 cm, volume 1400 cm^3) operable at 0–20 MPa and −50–100 ℃. Three matrix potential probes (Germanic GEO-Precision Environment Technology Company, Ettlingen, Germany) were embedded vertically at the top, middle, and bottom core positions in each medium; the height of each medium was 14 cm, and the depth of the three probes was 4, 8, and 12 cm.

Figure 1. Schematic diagram of the experimental apparatus [27]. Parts: 1. gas cylinder; 2. gas valve; 3. pressure gauge; 4. gas valve; 5. gas line; 6. reaction cell, height = 19.5 cm, diameter = 10.0 cm; 7. pF-meter sensors, length = 7 cm, diameter = 2 cm; 8. coolant temperature sensor; 9. low-temperature batch; 10. data-logging system of pressure value and coolant temperature; 11. data-logging system of pF value and temperature inside cell).

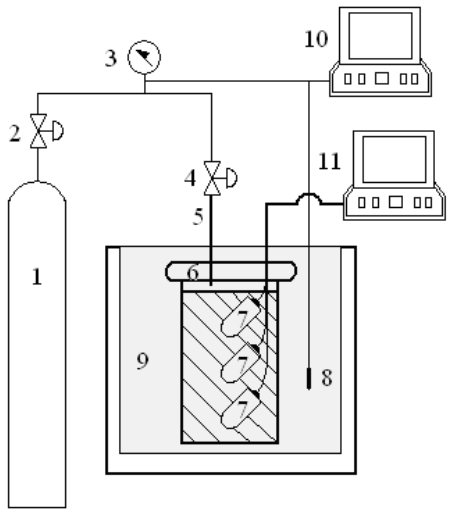

The system was evacuated for several minutes before the introduction of 99.99% pure methane gas (Hongzhuo Chemical Co., Ltd., Chengdu, China) into the reaction cell to the desired pressure, and then maintained at 12 ℃ for a period of time. Using a FP-50Hp low-temperature bath (−10~80 ± 0.05 ℃, JULABO Labortechnik GMBH, Seelbach, Germany), the system was uniformly cooled to 0.5 ℃ cover a period of 4h at a rate of about 0.048 ℃/min to form methane hydrate. During the reaction, the gas pressure (0~10 ± 0.02 MPa) was logged using a pressure transmitter (Model 5G081, Micro Sensor Co., Ltd., Baoji, China), and the matrix potential (0–10^7 mbar) and the temperature (−40~60 ± 0.05 ℃) were simultaneously logged by the matrix potential probes.

2.3. Experimental Standard Curve

Equations relating matrix potential and water content in each of the experimental media were used to construct standard curves for the silica gel and loess, as shown in Figures 2 and 3, respectively, which indicated that in the same medium, matrix potential was uniquely determined by water content.

Figure 2. Standard curve for the relationship between matrix potential and water content in silica gel.

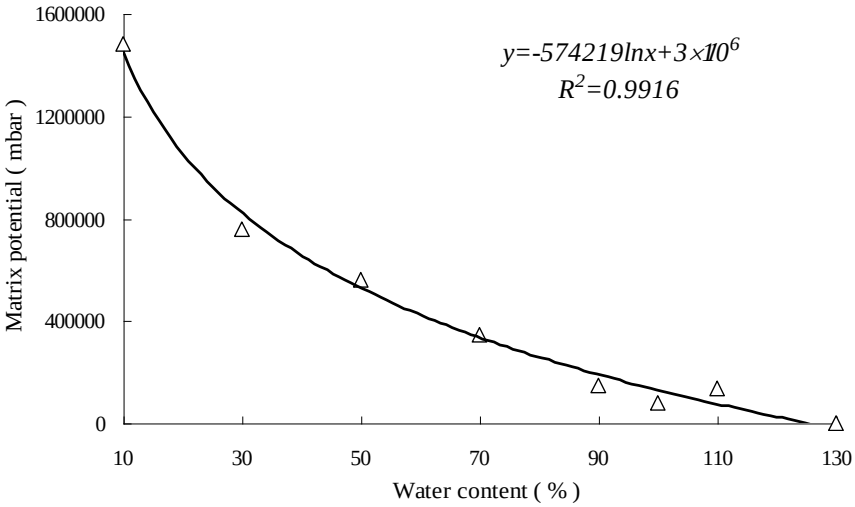

Figure 3. Standard curve for the relationship between matrix potential and water content in loess.

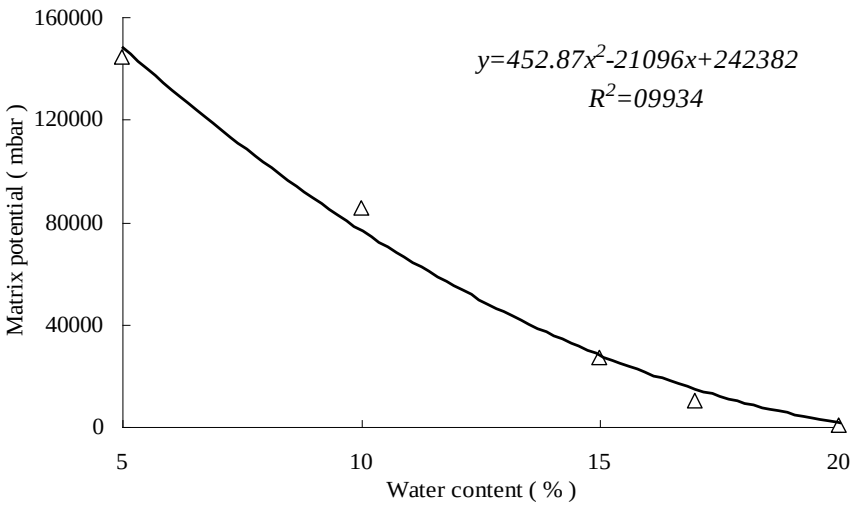

Equations (1) and (2) for calculating the matrix potential in silica gel and in loess, respectively, based on our many experimental results, are given below:

$$\text{Water content} = \exp\left[(\text{Matrix potential} - 3\times10^6)/-574219\right] - X_0 \tag{1}$$

$$\text{Water content} = \frac{21096 - \sqrt{21096^2 - 4\times452.87\times(242382 - \text{Matrix potential})}}{2\times452.87} - X_0 \tag{2}$$

where X_0 is the correction factor for linear drift. An important consideration is that the interaction potential between water and natural gas hydrate was significantly different from that between water and the original media (silica gel or loess), meaning that the relationship established in the absence of hydrate is not suitable for determining the water content in hydrate containing sediments. Based on the working principle of the probes, we applied the heat capacities, 4.19 J/g ·℃ and 2.04 J/g ·℃ (that of

ice) [28], respectively, and used the measured matrix potential values to accurately calculate the water conversion ratios during hydrate formation.

3. Results and Discussion

3.1. Methane Hydrate Formation in Artificial Medium

The changes in temperature, pressure, and matrix potential as functions of reaction time in hydrate formation in silica gel are shown in Figure 4. Upon cooling, the gas pressure fell precipitously. When the system reached 9.5 ℃ at about 5.1h, the temperature and the matrix potential as measured in all three positions rose substantially, indicating that methane hydrate began nucleating at that time and releasing a significant amount of heat, depleting the water present in the medium (Figure 2). The matrix potential continuously rose until the system cooled to 0.5 ℃, indicating that the hydrate continued to form throughout the matrix during that period. With stabilization of the temperature at 0.5 ℃, the gas pressure and the matrix potential also stabilized, indicating that the depletion of water in silica gel stopped according to the equations (1) and (2) and the formation reaction completed.

Figure 4. Changes in temperature, pressure, and matrix potential as functions of time in silica gel.

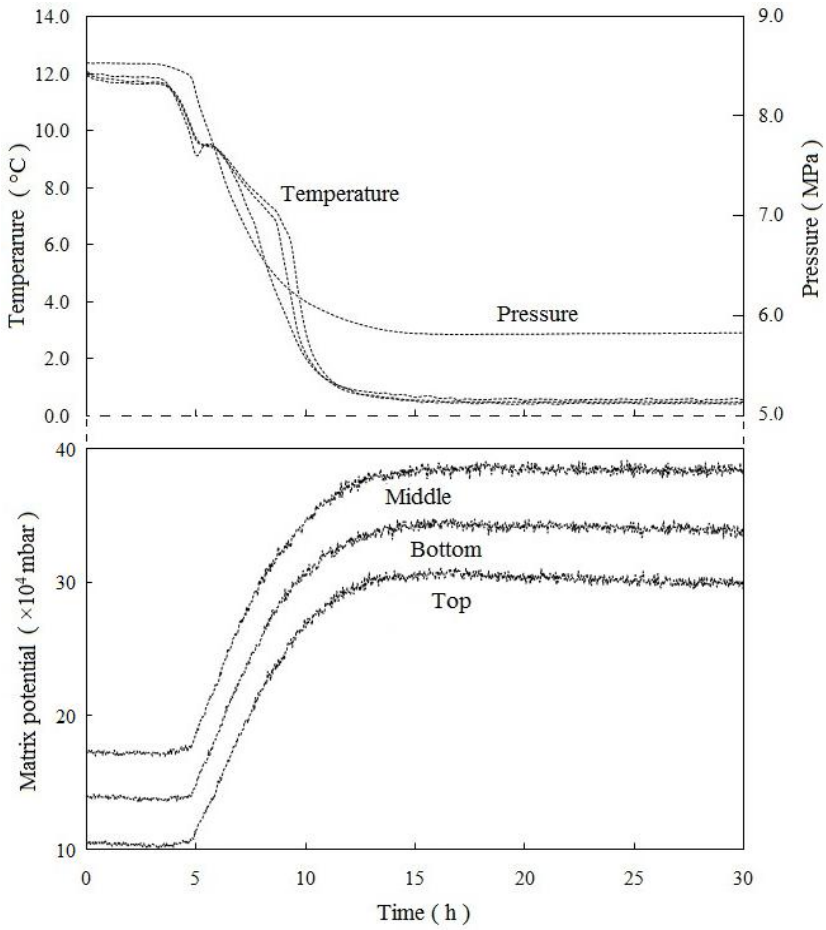

Using Equation (1), the water conversion ratios during the reaction in silica gel powder were calculated. The relationship between water conversion and reaction time is shown in Figure 5,

establishing that about 80% of the water was converted into methane hydrate. In addition, the graphs of the relationship between the water conversion ratio and reaction time as measured by the three sensors were all curved, indicating that the hydrate formation velocity was not constant during the reaction period. In order to examine these graphs more thoroughly, we divided the curves in Figure 5 into three time periods in accordance with their slope characteristics: 5–9 h, 9–15 h, and 15–30 h. Figures 6 and 7 show the relationship between water conversion ratios and reaction time over the 5–9 h and 9–15 h periods, respectively, confirming that the hydrate formation ratio as a function of reaction time was not constant.

Figure 5. Water conversion ratio as a function of reaction time in silica gel.

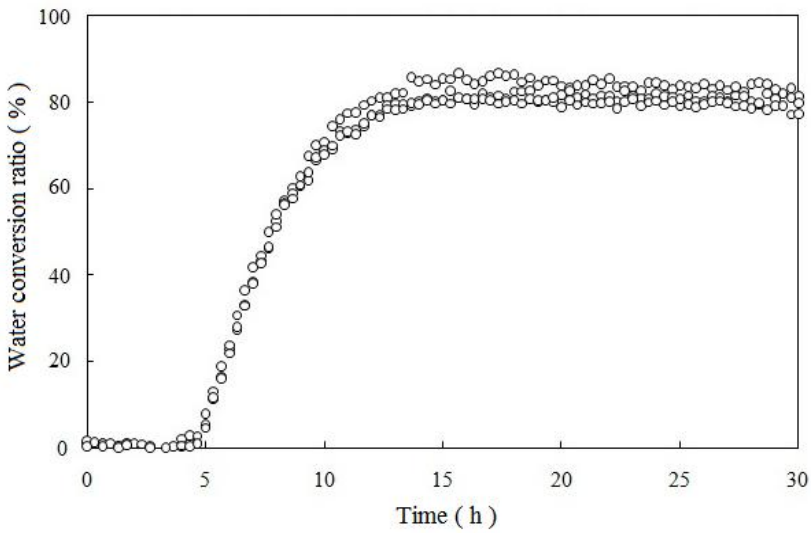

Figure 6. Amplitudes of the 5–9 h period in Figure 4 (for the compact linear regressions below, 5h, 9h in Figure 4 were respectively translated into 0 h, 4 h. Top: water conversion ratio = −0.0091× reaction time^2 + 0.1835 × reaction time + 0.0505, R^2 = 0.9987; Middle: water conversion ratio = −0.0175 × reaction time^2 + 0.2079 × reaction time + 0.0643, R^2 = 0.9975; Bottom: water conversion ratio = −0.0125 × reaction time^2 + 0.1918 × reaction time + 0.0462, R^2 = 0.9988. The reaction time only implies the horizontal axis in Figure 6).

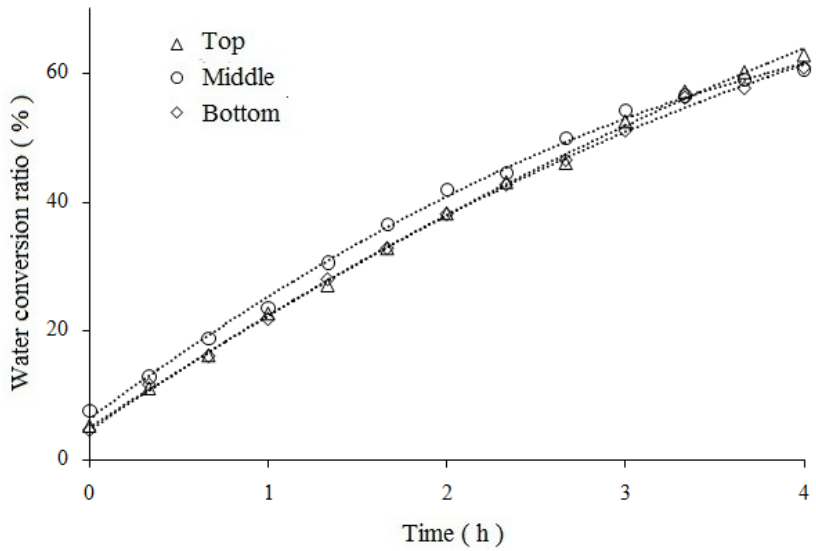

Figure 7. Amplitudes of 9–15 h period in Figure 4 (for the above same reasons, 9 h, 15 h in Figure 4 were respectively translated into 0 h, 6 h. Top: water conversion ratio = −0.0063 × reaction time^2 + 0.0709 × reaction time + 0.6496, R^2 = 0.9756; Middle: water conversion ratio = −0.007 × reaction time^2 + 0.0736 × reaction time + 0.6109, R^2 = 0.9809; Bottom: water conversion ratio = −0.0059 × reaction time^2 + 0.0654 × reaction time + 0.6196, R^2 = 0.9856. Reaction time implies the same as above).

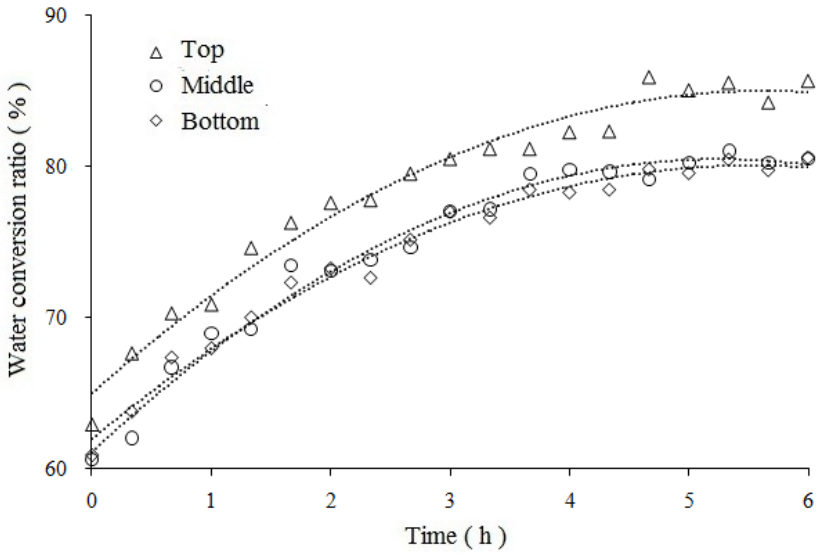

3.2. Methane Hydrate Formation in Natural Medium

Figure 8 shows the changes in temperature, pressure, and matrix potential in loess during the hydrate formation process. With cooling, the gas pressure fell substantially. When the system was cooled to about 8.0 ℃ at about 1.4 h, the temperature and matrix potential as measured in all three positions rose, indicating that methane hydrate began nucleating, releasing a significant amount of heat and depleting much of the water present (Figure 3). Contrary to the observations for the reaction in silica gel, there was a substantial reduction in the matrix potential with cooling, as shown in Figure 8. This reduction resulted from cooling of the reaction cell from the outside, which cause a significant amount of methane hydrate to form in the outer layer of loess and release heat; moreover, a large percentage of the loess particles (40.88% in Table 3) remained trapped within the largest pores (493.3–1869.4 Å), indicating that the water mobility in the loess was better than that in the silica gel. This indicates that the released heat from hydrate formation in loess drove some of the water to the center of the medium and caused the matrix potential to fall. When methane hydrate began forming in the center of the loess, the water was depleted and the matrix potential rose. While the temperature remained stable at 0.5 ℃ after the cooling process was finished, the gas pressure continued to fall and the matrix potential continued to rise, indicating that depletion of water in silica gel continued, according to Equations (1) and (2), and hydrate formation was progressing.

Figure 8. Temperature, pressure, and matrix potential changes as functions of reaction time in loess.

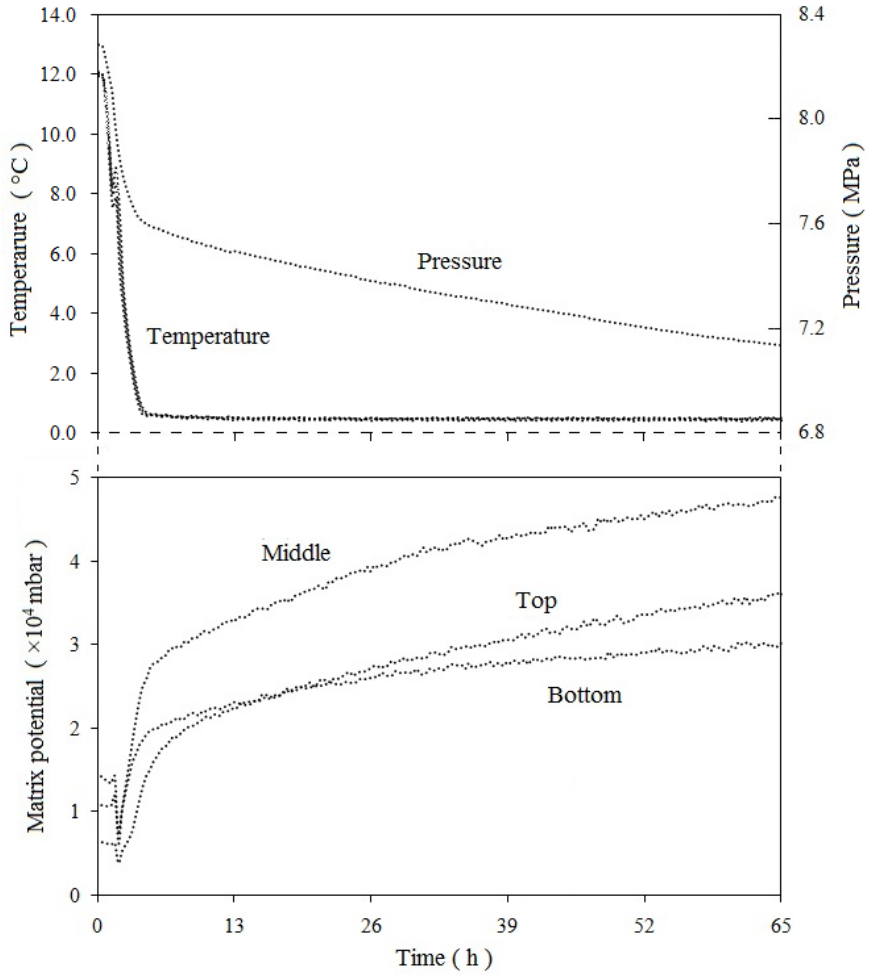

Using Equation (2), the water conversion ratios as functions of hydrate formation reaction time in loess were calculated, as shown in Figure 9. After fully cooling, about 10%, 20%, 26% of water corresponding to "Middle", "Bottom", "Top" in Figure 9 was respectively converted into methane hydrate. At the beginning of the reaction, heat releasing from hydrate formation drove some water into the medium center, which was discussed in the above section, and made the conversion ratios of water negative at that time. However, the water conversion ratios continued to rise even after the temperature stabilized, indicating that the formation of methane hydrate continued during that period. Similar to the reaction in silica gel, the graphs representing the relationship between the water conversion ratios and the reaction time for loess were curved. We divided these curves into three time periods: 2–5, 5–15.5, and 15.5–65 h. Figures 10, 11, and 12 show the relationship between the water conversion ratios and the reaction time in the three time periods, all of which are curved, indicating that the formation ratios as functions of reaction time were not constant.

Figure 9. Water conversion ratio as a function of reaction time in loess.

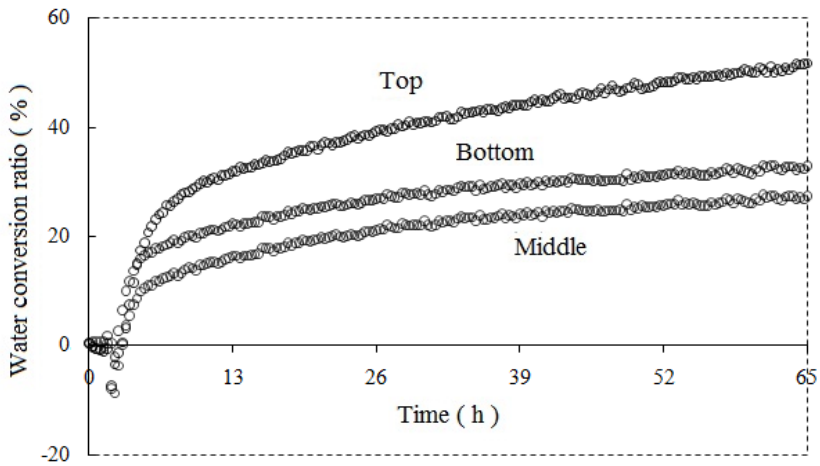

Figure 10. Amplitudes of 2–5 h period in Figure 9 (for the same reason as in Figure 6, 2 h, 5 h in Figure 9 were respectively translated into 0 h, 3 h. Top: water conversion ratio = 0.0017 × reaction time^2 + 0.0868 × reaction time – 0.0426, $R^2 = 0.9864$; Middle: water conversion ratio = −0.027 × reaction time^2 + 0.1414 × reaction time − 0.0833, $R^2 = 0.9969$; Bottom: water conversion ratio = −0.026 × reaction time^2 + 0.1368 × reaction time − 0.0166, $R^2 = 0.9969$. Reaction time only implies the horizontal axis in Figure 10).

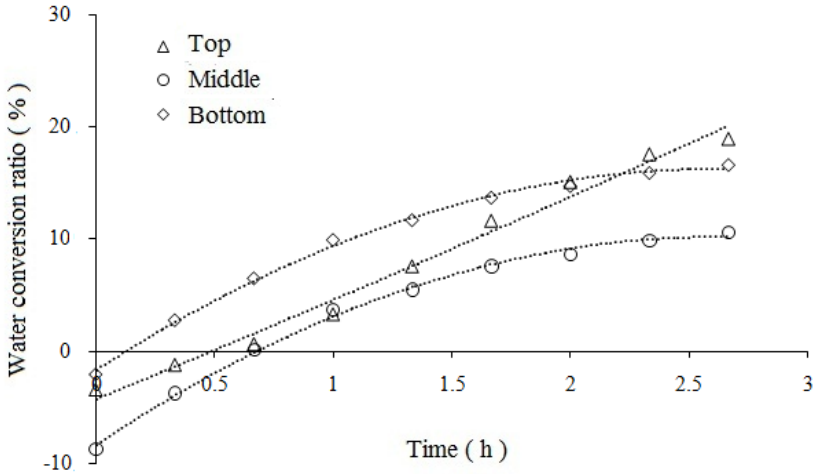

Figure 11. Amplitudes of 5–15.5 h period in Figure 9 (for the same reason as above, 5 h, 15.5 h in Figure 9 were respectively translated into 0 h, 10.5 h. Top: water conversion ratio = −0.0011 × reaction time^2 + 0.0237 × reaction time + 0.2053, R^2 = 0.9829; Middle: water conversion ratio = −0.0003 × reaction time^2 + 0.009 × reaction time + 0.1075, R^2 = 0.9793; Bottom: water conversion ratio = −0.0003 × reaction time^2 + 0.0087 × reaction time + 0.1679, R^2 = 0.9793. Reaction time implies the same as above).

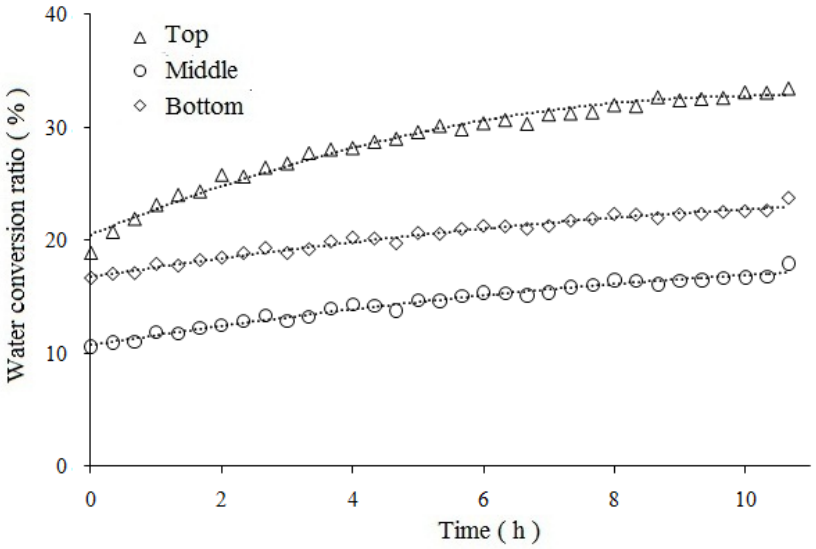

Figure 12. Amplitudes of 15.5–65 h period in Figure 9 (for the same reason as above, 15.5 h, 65 h in Figure 8 were respectively translated into 0 h, 50 h. Top: water conversion ratio = −0.00003 × reaction time^2 + 0.0052 × reaction time + 0.3395, R^2 = 0.9954; Middle: water conversion ratio = −0.00003 × reaction time^2 + 0.0032 × reaction time + 0.18, R^2 = 0.9795; Bottom: water conversion ratio = −0.00003 × reaction time^2 + 0.0031 × reaction time + 0.238, R^2 = 0.9795. Reaction time implies the same as above.)

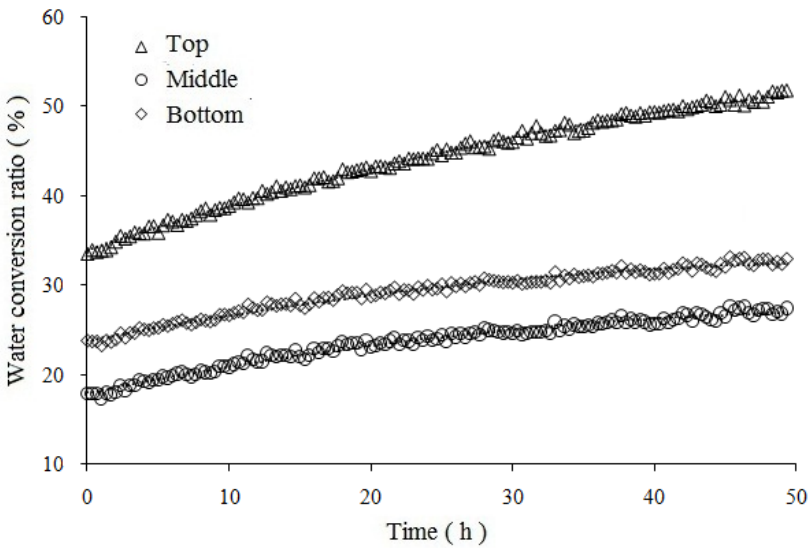

3.3. Comparison of Methane Hydrate Formation in Silica Gel and in Loess

The experimental results indicate that there are both similarities and differences between the reactions in artificial and natural media. In the two media, methane hydrates were both formed among particles of medium depressively and consolidated each medium rigidly, with morphology which looked like frozen by frost. The relationship between the water conversion ratios and the reaction time for both conditions displayed quadratic equation characteristics, as shown in Figures 6, 7, 10, 11, and 12. The first-order derivative of each of the equations was calculated, and the results indicated that both reactions gradually decelerated, indicating that hydrate formation relied on water transfer to the hydrate surfaces with lower Gibbs free energy [29] after nucleation.

The differences between the reactions in the two media were more obvious. The final water conversion ratio in silica after cooling was about 80% (Figure 5), as compared to only about 30% conversion in loess (Figure 9). The water saturations of the two media were approximately 71% in silica gel and 72% in loess, calculated with the data in Table 1. However, the surface area of silica gel at 499.423 m^2/g (Table 2) was more than 60 times that of loess 7.926 m^2/g (Table 3). Considering the fact that the water volume of 600 cm^3 (Table 1) in silica gel was only about three times that (198 cm^3) (Table 1) in loess, we speculated that there were far more nucleation points in silica gel than in loess and the water films capsuling the particles of silica gel were much thinner than that of loess, so methane gas was easier dissolved into water within silica gel under the same gas pressure and temperature cooling conditions as within loess and it is unsurprising that greater amounts of methane hydrate were formed in silica gel. The progression of the reaction in each type of media was also quite different, as the duration of the reaction in silica gel was only 14 h (Figure 5), while that in loess took more than 65 h. This indicates that the formation reactions were significantly affected by the lithology of the media. Because the silica gel powder had a very large internal surface area and a uniform pore size distribution (Table 2), its water retention capacity was very high and its lithology was homogeneous. As such, methane hydrate formed readily in silica gel in a short, intense reaction that generated a large amount of product. In contrast, the pore size distribution of loess was far more heterogeneous (Table 3), meaning that the hydrate formation gradually penetrated the medium from the larger pores to the smaller pores [30]. Therefore, the formation reaction in loess required a very long time to achieve completion. During that time (Figure 12), the hydrate formation in loess relied on water transfer to the hydrate surfaces, causing the reaction to gradually decelerate. Compared with the reaction in silica gel, that in loess was much slower and formed less product.

Additionally, although the water saturations in the two media were similar, 71% in silica gel and 72% in loess, the water bearing matrix potential 1.1–1.7 $\times 10^5$ mbar in silica gel in Figure 4 was much higher than that 0.6–1.5 $\times 10^4$ mbar in loess in Figure 8, which indicated that water in loess was enduring much lighter suction caused by complicated physical properties of a medium matrix and constrained more weakly by the adsorption and capillary function derived from the soil micro particles and therefore had stronger fluidity. Based on the more obvious fluidity in loess, the water conversion ratios in top, middle and bottom presented different tendencies between in artificial and in natural media. And the more detailed studies on the differences of water conversion ratios related to water fluidity and positions will be conducted in our next work in future.

4. Conclusions

It is well known that physical properties of gas hydrate-bearing sediments can be obviously affected by porosity, water content, *etc.* [6,7] and configurations and properties of natural media are very complicated and can't be completely calculated and simulated mathematically [17]. However, water within sediment bearing the suction derived from the soil micro particles and complicated physical properties of medium can be defined as the matrix potential in agrology and quantitatively measured by some apparatuses (*i.e.*, pF-meter sensors in this paper). So, the experimental water contents of media were determined based on the matrix potential of media in this work, in spite of the water contents of the different media listed in Table 1. And the relationship between the matrix potential and the water content during the formation of methane hydrate in different media was determined accurately using established equations. By generating standard curves for these relationships and applying the heat capacity of water (4.19 J/g ·℃) and of methane hydrate (2.04 J/g ·℃), the water conversion ratios during methane hydrate formations were calculated. The characteristics of the formation reactions in artificial and natural media were studied. The formation of methane hydrate in the two media was divided into three time periods: rapid formation, buffer formation, and termination. Over the course of the formation processes, the reaction velocity of hydrate nucleation decelerated because hydrate growth relied on water transfer to the hydrate surfaces with lower Gibbs free energy after nucleation. Significant differences in the progression of methane hydrate formation were observed and attributed to the differences in water retention capacity and lithology in the two media. The larger surface area of the artificial medium (silica gel) provided far more nucleation points, enabling a much faster formation rate of methane hydrate. The greater pore size distribution of the natural medium (loess) obligated a gradual penetration of the water from larger to smaller pores, extending the reaction duration considerably. From these results, we speculate that in nature, the sediment lithology has a significant impact on the formation conditions and the reaction characteristics of gas hydrates.

Acknowledgements

We are grateful for the financial support from the Youth Science Foundation (Grant No. 41101070), the CAS West Action Plan (Grant No. KZCX2-XB3-03), the Foundation for Excellent Youth Scholars of CAREERI, CAS (Grant No. 51Y184A41), and the Project for Incubation of Specialists in Glaciology and Geocryology of the National Natural Science Foundation of China (J0930003/ J0109).

References

1. Sloan, E.D. Fundamental principles and applications of natural gas hydrates. *Nature* **2003**, *426*, 353–359.
2. Kvenvolden, K.A. Methane hydrates—A major reservoir of carbon in shallow Geosphere. *Chem. Geol.* **1988**, *71*, 41–51.
3. Kvenvolden, K.A. Potential effects of gas hydrate on human welfare. *Proc. Natl. Acad. Sci. USA* **1999**, *96*, 3420–3426.
4. Collett, T.S. Energy resource potential of natural gas hydrate. *APG Bull.* **2002**, *86*, 1971–1992.

5. Handa, Y.P.; Stupin, D. Thermodynamic properties and dissociation characteristics of methane and propane hydrates in 70-Å radius silica gel pores. *J. Phys. Chem.* **1992**, *96*, 8599–8603.
6. Waite, W.F.; Winters, W.J.; Mason, D.H. Methane hydrate formation in partially water-saturated ottawa sand. *Am. Mineral.* **2004**, *89*, 1202–1207.
7. Waite, W.F.; de Martin, B.J.; Kirby, S.H.; Pinkston, J.; Ruppel, C.D. Thermal conductivity measurements in porous mixtures of methane hydrate and quartz sand. *Geophys. Res. Lett.* **2002**, *29*, 2229, doi:10.1029/2002GL015988.
8. Anderson, B.; Llamedo, M.; Tohidi, B. Characteristics of clathrate hydrate equilibria in mesopores and interpretation of experimental data. *J. Phys. Chem. B.* **2003**, *107*, 3500–3506.
9. Anderson, B.; Llamedo, M.; Tohidi, B. Experimental measurement of methane and carbon dioxide clathrate hydrate equilibria in mesoporous silica. *J. Phys. Chem. B.* **2003**, *107*, 3507–3514.
10. Buffett, B.A.; Zatsepina, O.Y. Formation of gas hydrate from dissolved gas in natural porous medium. *Mar. Geol.* **2000**, *164*, 69–77.
11. Klauda, J.B.; Sandler, S.I. Modeling gas hydrate phase equilibria in laboratory and natural porous medium. *Ind. Eng. Chem. Res.* **2001**, *40*, 4197–4208.
12. Klauda, J.B.; Sandler, S.I. Predictions of gas hydrate phase equilibria and amounts in natural sediment porous medium. *Mar. Pet. Geol.* **2003**, *20*, 459–470.
13. Ostergaard, K.K.; Anderson, R.; Llamedo, M.; Tohidi, B. Hydrate phase equilibria in porous media: effect of pore size and salinity. *Terra Nova* **2002**, *14*, 307–312.
14. Uchida, T.; Ebinuma, T.; Ishizaki, T. Dissociation condition measurements of methane hydrate in confined small pores of porous glass. *J. Phys. Chem. B* **1999**, *103*, 3659–3662.
15. Uchida, T.; Ebinuma, T.; Takeya, S.; Nagao, J.; Narita, H. Effects of pore sizes on dissociation temperatures and pressures of methane, carbon dioxide and propane hydrate in porous media. *J. Phys. Chem. B* **2002**, *106*, 820–826.
16. Wilder, J.W.; Seshadri, K.; Smith, D.H. Modeling hydrate formation in medium with broad pore size distribution. *Langmuir* **2001**, *17*, 6729–6735.
17. Rempel, A.W. A model for the diffusive growth of hydrate saturation anomalies in layered sediments. *J. Geophy. Res.* **2011**, *116*, 1–15.
18. Rempel, A.W; Wettlaufer J.S.; Worster M.G. Interfacial pre-melting and the Thermomolecular force: Thermodynamic buoyancy. *Phys. Rev. Lett.* **2001**, *87*, 088501.
19. Clarke, A.M.; Pooladi-Darvish, M.; Bishnoi, P.R. A method to predict equilibrium conditions of gas hydrate formation in porous media. *Ind. Eng. Chem. Res.* **1999**, *38*, 2485–2490.
20. Andersland, O.B.; Ladanyi, B. *An Introduction to Frozen Ground Engineering*; Chapman and Hall: New York, NY, USA, 2004.
21. Dash, J.G.; Rempel, A.W.; Wettlaufer, J.S. The physics of premelted ice and its geophysical consequences. *Rev. Mod. Phys.* **2006**, *78*, 695–741.
22. Hansen-Goos, H.; Wettlaufer, J.S. Theory of ice premelting in porous media. *Phys. Rev. E* **2010**, *81*, 031604, doi:10.1103/PhysRevE.81.031604.
23. Chuvilin, E.; Yakushev, V.S.; Perlova, E.V. Experimental study of gas hydrate formation in porous media. *Adv. Cold Reg. Therm. Eng. Sci.* **1999**, *533*, 431–440.

24. Chuvilin, E.; Guryeva, O. Carbon Dioxide Gas Hydrates Accumulation in Freezing and Frozen Sediments. In *Proceedings of the 6th International Conference on Gas Hydrates (ICGH 2008)*, British Columbia, Canada, 6–10 July, 2008.
25. Chuvilin, E.; Guryeva, O.; Istomin V.; Safonov. S. Experimental Method for Determination of the Residual Equilibrium Water Content in Hydrate-Saturated Natural Sediments. In *Proceedings of the 6th International Conference on Gas Hydrates (ICGH 2008)*, British Columbia, Canada, 6–10 July 2008.
26. Kawasaki, T.; Tsuchiya, Y.; Nakamizu, M. Observation of Methane Hydrate Dissociation Behavior in Methane Hydrate Bearing Sediments by X-Ray CT Scanner. In *Proceedings of the 5th International Conference on Gas Hydrates*, Trondheim, Norway, 12–16 June 2005.
27. Zhang, P.; Wu, Q.B.; Pu, Y.B.; Jiang, G.L.; Zhan, J.; Wang, Y.M. Water transfer characteristics during methane hydrate formation and dissociation processes in saturated sand. *J. Nat. Gas Chem*. **2010**, *19*, 71–76.
28. Sloan, E.D. Molecular Structures and Similarities. *Clathrate Hydrates of Natural Gases*, 2nd ed.; CRC Press: New York, NY, USA, 1998; p. 60.
29. Sloan, E.D. Kinetics of Hydrate Formation. *Clathrate Hydrates of Natural Gases*, 2nd ed.; CRC Press: New York, NY, USA, 1998; p. 111.
30. Clennell, M.B.; Hovland, M.; Booth, J.S. Formation of natural gas hydrates in marine sediments: 1. Conceptual model of gas hydrate growth conditioned by host sediment properties. *J. Geophys. Res.* **1999**, *104*, 22985–23003.